Slope Traversability Analysis of Reconfigurable Planetary Rovers

Hiroaki Inotsume, Masataku Sutoh, Kenji Nagaoka, Keiji Nagatani, and Kazuya Yoshida

***Abstract*— Future planetary rovers are expected to probe over steep sandy slopes, such as crater rims, where wheel slippage can be a critical issue. One solution to this issue is to mount redundant actuators on the locomotion mechanisms of the rovers such that they can actively reconfigurate themselves to adapt to the driven terrain. In this study, we propose a mechanical model of a rover based on a wheel-soil contact model combined with the classical terramechanic theory. The effects of the rover reconfiguration on its slippage tendencies are analyzed based on slope traversing experiments and numerical simulations. The validation of the proposed contact model is also discussed based on experimental and numerical simulation results. According to the experimental results, both longitudinal and lateral slippages are greatly reduced by tilting the rover in an uphill direction. The results of the numerical simulation match the experimental results quantitatively, and indicate the possible need to include a slope failure model.**

I. Introduction

The success of NASA's MER Mission has validated the usefulness of rovers for planetary surface exploration, and elevated the expectations of future rover exploration missions. Consequently, rovers designed for future missions are expected to probe more challenging terrain, such as the rims or insides of craters. However, since the surfaces of the Moon and Mars are covered with fine-grained sand, when rovers traverse the slopes of their craters, wheel slippages can easily occur in both longitudinal and lateral direction becoming a critical issue. Therefore, future exploration rovers will require higher mobility on such terrain.

In recent years, rovers that can actively modify their configuration to adapt to rough environments have attracted considerable attention. Such rovers are called "reconfigurable robots" [2], and several studies have proved their potential to negotiate challenging terrain. Studies on reconfigurable rovers have thus far primarily focused on an improvement of their traction or rollover stability on rough terrain [1]-[3]. On the other hand, Wettergreen et al. [4] showed experimentally that a downhill sideslip can be reduced by tilting a rover along the uphill direction when the rover traverses sandy slopes. However, the relationship between such attitude change and a downhill sideslip has not been sufficiently analyzed. If the forces between the wheels and soil are estimated, a sideslip can be minimized on arbitrary slopes by optimizing the rover configuration. To achieve this, a wheel-soil contact model is needed to analyze complicated interactions between the wheels and soil.

Wheel-soil interactions have been studied in the field of "terramechanics" [5], [6], and have recently been applied to mobility problems in planetary rovers (e.g., [7]-[9]). Our research group has also been studying mobility of planetary rovers based on terramechanics [10]-[12]. Nonetheless, the terramechanical theory has mainly been applied to wheels making vertical contact with the soil and not to a mobility analysis of reconfigurable rovers whose wheels can make sidling contact with the soil.

In this paper, based on terramechanics and slope traversing experiments using a wheeled rover, we analyzed the effects of the rover reconfiguration on slippages occurring over sandy deformable slopes while the rover laterally traverses. Section II describes the traversability criteria used for a deformable side slope. A mechanical model of the rover is also introduced in this section. In Section III, a wheel-soil interaction model for a wheel inclined over a sandy slope is proposed based on the terramechanical theory. In Section IV, the traversability for a reconfigurable rover is analyzed based on slope traversing experiments and numerical simulations. Finally, the results of the experiments and simulations are compared, and the validation of the proposed rover model is discussed.

II. Slope Traversability for a Rover

A. Traversability Criteria

In this study, "slip ratio" and "slip angle" are used as slope traversability criteria.

Fig. 1 illustrates a rover laterally traversing a sandy slope with an angle of α. The rover and its wheels are tilted angle of ψ_h in an uphill direction from the vertical contact with the slope (see Fig. 2). In Fig. 1, the slope coordinate system, Σ_s, is defined as follows: $x^{(s)}$ denotes the desired traversing direction, $y^{(s)}$ denotes the uphill direction, and $z^{(s)}$ denotes the vertically upward direction against the slope surface, as a right-handed system. Here, we assume that any orientation errors of the rover from the desired direction are negligible, and that the heading of the rover is along the $x^{(s)}$ axis. The rover coordinate system, Σ_r, is then obtained through a rotation of Σ_s about the $x^{(s)}$ axis with ψ_h. In addition, the wheel coordinate system, Σ_{wi} (where i is the wheel number), is defined at the center of the wheel. In this study, Σ_{wi} is not rotated from Σ_r and is simply shifted from the COG of the rover to the center of each wheel.

Slip ratio, s, is a proportion of the desired and actual traveling speeds as follows [6]:

$$s = 1 - \frac{v_x}{r\omega} \qquad (0 \leq s \leq 1), \tag{1}$$

where v_x denotes the actual traveling speed along the $x^{(r)}$ axis, and r and ω denote the radius and angular velocity of

The authors are with the Department of Aerospace Engineering, Tohoku University, Aoba 6-6-01, Sendai, 980-8579, Japan, {inotsume, sutoh, nagaoka, keiji, yoshida}@astro.mech.tohoku.ac.jp

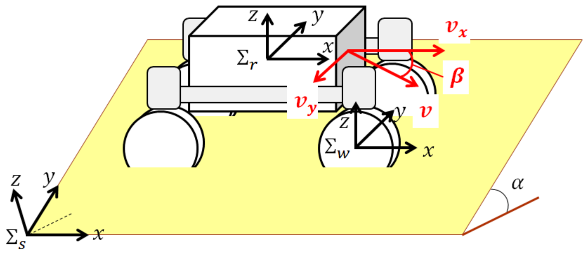

Fig. 1. Definition of coordinate systems

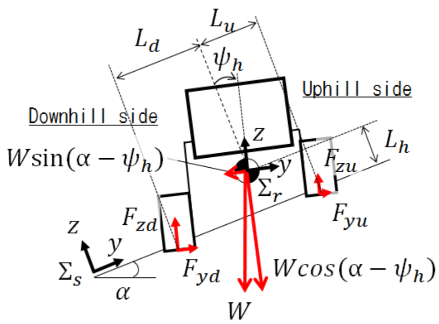

Fig. 2. Mechanical rover model on a side slope

the wheel, respectively. The slip ratio represents the degree of longitudinal slippage.

On the other hand, lateral slippage is expressed using the slip angle. Slip angle, β, is given as the angle between the heading velocity, v_x, and the traveling velocity, v [11]:

$$\beta = \tan^{-1}\left(\frac{v_y}{v_x}\right), \tag{2}$$

where v_y denotes the lateral velocity of the rover along the $y^{(r)}$ axis due to side slippage.

The smaller the value of $|s|$ and $|\beta|$ are, the greater the traversabiity for the rover is.

B. Mechanical Model of a Reconfigurable Rover

As shown in Fig. 2, we assume that the COG of the rover is located at a height of L_h along the $z^{(s)}$ axis and at distances of L_u and L_d away from the uphill and downhill wheels along the $y^{(s)}$ axis, respectively. Here, forces acting on the front and rear wheels are equivalent and the rover traverses under a steady state. Consequently, the load acting on the uphill and downhill wheels due to the gravitational force are calculated as follows:

$$Uphill\ side: \quad W_u = \frac{W(L_d\cos\alpha - L_h\sin\alpha)}{2(L_u + L_d)\cos\alpha}, \tag{3}$$

$$Downhill\ side: W_d = \frac{W(L_u\cos\alpha + L_h\sin\alpha)}{2(L_u + L_d)\cos\alpha}, \tag{4}$$

where W denotes the weight of the rover. In addition, the following equations are obtained for each wheel i:

$$F_{xi} = 0, \tag{5}$$

$$F_{yi} = W_i \sin\alpha', \tag{6}$$

$$F_{zi} = W_i \cos\alpha', \tag{7}$$

where F_{xi}, F_{yi}, and F_{zi} are the drawbar pull, side force, and vertical force acting on each wheel from the soil along the $x^{(w)}$, $y^{(w)}$, and $z^{(w)}$ directions, respectively. Besides, $\alpha' = \alpha - \psi_h$. Therefore, the whole forces acting on the rover are expressed as a summation of forces acting on each wheel:

$$\left.\begin{aligned} 2\left(F_{xu} + F_{xd}\right) &= 0, \\ 2\left(F_{yu} + F_{yd}\right) &= W\sin\alpha', \\ 2\left(F_{zu} + F_{zd}\right) &= W\cos\alpha'. \end{aligned}\right\} \tag{8}$$

III. Wheel-Soil Contact Model for a Slope

The above-mentioned forces, F_x, F_y, and F_z, result from a complicated wheel-soil interaction. In this section, such interaction is modeled based on terramechanics.

A. Wheel-Soil Contact Forces

Fig. 3 depicts a wheel traversing along a sandy slope. In the figure, the wheel contacts with a slope tilted γ toward the uphill direction. As mentioned above, when the wheel drives on the soil, wheel-soil interaction forces, F_j $(j = x, y, z)$, act on the wheel. These forces are composed of two different kinds of forces: forces acting on the bottom part of the wheel due to shearing, F_{jb}, and forces acting on the sidewall of the wheel, F_{js}:

$$F_j = F_{jb} + F_{js}. \tag{9}$$

B. Forces Acting on Bottom Part of the Wheels

When a wheel drives on loose soil, normal stress, σ, and tangential and lateral shear stresses, τ_t and τ_l, act on the bottom surface of the wheel as shown in Fig. 4. The component of forces, F_{jb} $(j = x, y, z)$, on the bottom surface are given by integrating the j directional component of the stresses along the wheel circumference.

As shown in Fig. 5, we first slice the wheel into wheel elements with very small width of dy along the $y^{(w)}$ direction. Forces acting on the sliced wheel element at the y position, dF_{jb}, are given as follows [6], [11]:

$$dF_{xb}(y) = r dy \int_{\theta_r}^{\theta_f} \{\tau_t \cos\theta - \sigma\sin\theta\} d\theta, \tag{10}$$

$$dF_{yb}(y) = r dy \int_{\theta_r}^{\theta_f} \tau_l d\theta, \tag{11}$$

$$dF_{zb}(y) = r dy \int_{\theta_r}^{\theta_f} \{\tau_t \sin\theta + \sigma\cos\theta\} d\theta, \tag{12}$$

where r is the wheel radius, and θ_f, θ_r are the entry and exit angles of the wheel at y. The whole forces acting on the bottom surface, F_{jb}, are then derived by integrating these forces along the $y^{(w)}$ direction [17]:

$$F_{jb} = \int_{-b/2}^{b/2} dF_{jb}(y). \tag{13}$$

The parameters needed to calculate these forces are the wheel sinkage (along with the entry and exit angles) and wheel-soil stresses. These factors are described below.

Wheel sinkage: As illustrated in Fig. 6, the total sinkage at position y, $h'_0(y)$, is given as follows:

$$h'_0(y) = y\tan\gamma + h'_c, \tag{14}$$

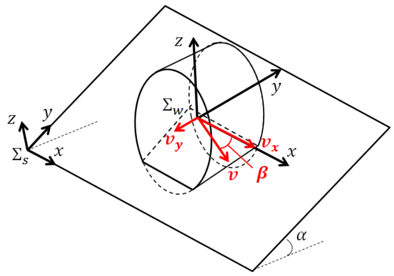

Fig. 3. Wheel coordinate system on a lateral slope

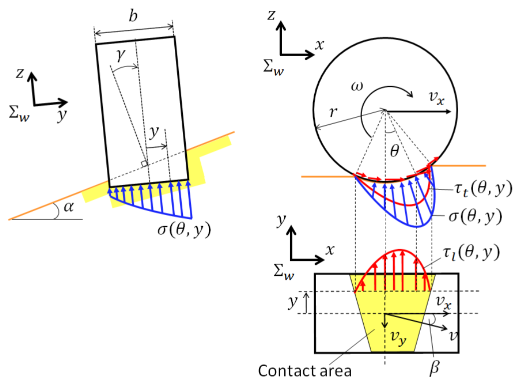

Fig. 4. Normal and shear stresses beneath a wheel

where h'_c is the total sinkage at the center of the wheel (i.e., $y = 0$). Note that h'_0 is the sinkage in the wheel coordinate system, Σ_w, and differs from the vertical sinkage, h_0. The wheel entry and exit angles at position y, $\theta_f(y)$ and $\theta_r(y)$, are given using $h'_0(y)$:

$$\theta_f(y) = \cos^{-1}(1 - h'_0(y)/r), \tag{15}$$

$$\theta_r(y) = \cos^{-1}(1 - \lambda h'_0(y)/r), \tag{16}$$

where, λ denotes the exit angle coefficient which depends on the soil, wheel characteristics and slip ratio s [11].

Wheel-soil stresses: Normal stress acting on an arbitrary point on the wheel surface (θ, y) is given by using Reece's pressure-sinkage relationship [13]:

$$\sigma(\theta, y) = \begin{cases} (ck_c + \rho g l_w k_\phi)\left(\frac{r}{l_w}\right)^n (cos\theta - cos\theta_f)^n \\ \qquad (\theta_m \le \theta < \theta_f), \\ (ck_c + \rho g l_w k_\phi)\left(\frac{r}{l_w}\right)^n \times \\ \left[\left(\cos\{\theta_f - \frac{(\theta-\theta_r)(\theta_f-\theta_m)}{\theta_m-\theta_r}\} - \cos\theta_f\right)\right]^n \\ \qquad (\theta_r \le \theta < \theta_m), \end{cases} \tag{17}$$

where ρ denotes the soil bulk density; c denotes cohesion; k_c, k_ϕ, and n denote the pressure-sinkage moduli of the soil; and g denotes the acceleration of gravity. In addition, l_w expressed as $l_w = \min(l_c, b_e)$ [14] denotes the smaller of the two dimensions of the wheel-soil contact patch, where l_c denotes the length of the contact patch and b_e denotes the effective wheel width, or actual contact width. Finally, θ_m is the specific wheel angle at which the normal stress is at maximum and is expressed following the empirical formula below using soil-specific parameters, a_0 and a_1 [15]:

$$\theta_m(y) = (a_0 + a_1 s)\theta_f(y). \tag{18}$$

There are several methods used to express tangential and lateral shear stresses. A commonly used method gives these

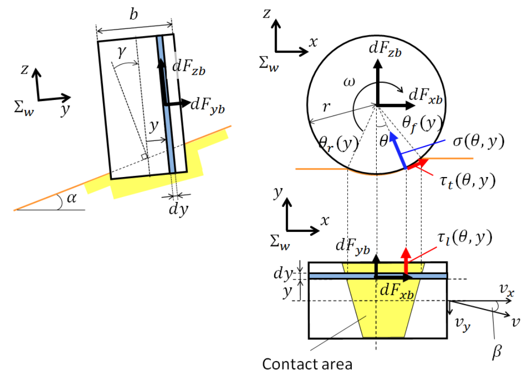

Fig. 5. Forces acting on a sliced wheel element

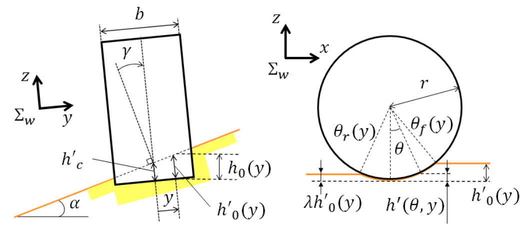

Fig. 6. Sinkage of a tilted wheel on a slope

two shear stresses independently; however, there are potential problems with this (e.g., the total shear stress can be exceed the maximum soil strength value). Hence, we use another method to calculate the shear stresses. First, we obtain the total stress τ at point (θ, y) as follows [16]:

$$\tau(\theta, y) = (c + \sigma(\theta, y)\tan\phi)\left(1 - \exp(-j(\theta)/k)\right), \tag{19}$$

where ϕ denotes the internal friction angle of the soil, and k denotes the shear deformation modulus which depends on the soil and wheel shape. j denotes the total soil deformation and $j = \sqrt{j_t^2 + j_l^2}$. Tangential and lateral soil deformation, j_t and j_l, are given as follows [11]:

$$j_t(\theta, y) = r\{(\theta_f - \theta) - (1 - s)(\sin\theta_f - \sin\theta)\}, \tag{20}$$

$$j_l(\theta, y) = -r(1 - s)(\theta_f - \theta)\tan\beta. \tag{21}$$

The tangential and lateral shear stress, τ_t and τ_l, are then given as [15]

$$\tau_{t,l}(\theta, y) = \left(v_{jt,l}/\sqrt{{v_{jt}}^2 + {v_{jl}}^2}\right) \cdot \tau(\theta, y), \tag{22}$$

where v_{jt} and v_{jl} are the tangential and lateral slip velocities of the soil, respectively, and are obtained from the following equations [11]:

$$v_{jt}(\theta) = r\omega\left\{1 - (1 - s)\cos\theta\right\}, \tag{23}$$

$$v_{jl}(\theta) = -r\omega(1 - s)\tan\beta. \tag{24}$$

C. Forces Acting on Wheel Sidewall

In this study, we assume that active and passive soil resistances act on the sidewall of the wheel when a sideslip occurs on a slope. Herein, we approximate the soil failure pattern using a flat plane as illustrated in Fig. 7. Consequently, the passive and active soil resistances are calculated based on the fundamental idea of the soil cutting resistance [19]. According to Reece's fundamental earthmoving theory [20],

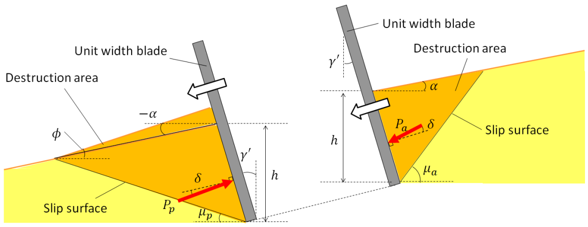

Fig. 7. Passive and active soil resistances on the sidewall

soil cutting resistances of an unit width blade are expressed as follows:

$$P = \rho g h^2 N_\rho + chN_c + c_a hN_{ca} + gqN_q, \tag{25}$$

where c_a denotes adhesion between the wall and soil, and q is surcharge stress over the soil surface. N_ρ, N_c, N_{ca}, and N_q are parameters dependent on the soil character, and geometry of the terrain and the wall.

Passive soil resistance P_p acts on the sidewall, which bulldozes soil as shown in Fig. 7. We assume that bulldozed soil accumulates at the front of the sidewall. Thus, P_p is given as follows:

$$\left.\begin{array}{l}
P_p = \rho g h^2 N_\rho + chN_c + c_a hN_{ca}, \\
N_\rho = \dfrac{C\left\{1+\frac{\cos(\mu_p-\gamma')\sin(\phi+\alpha)}{\cos(\gamma'+\phi)\sin(\mu_p-\alpha)}\right\}}{2C_p \sin(\mu_p-\alpha)\cos\gamma'}, \\
N_c = -\dfrac{\{\sin\mu_p+\cos\mu_p\cot(\mu_p+\phi)\}\cos(\gamma'-\alpha)}{C_p}, \\
N_{ca} = -\dfrac{\cos\gamma'-\sin\alpha\cot(\mu_p+\phi)}{C_p}, \\
C = \cos(\mu_p-\gamma')\cos(\gamma'-\alpha), \\
C_p = \cos\gamma'\{\sin(\gamma'-\delta)+\cos(\gamma'-\delta)\cot(\mu_p+\phi)\},
\end{array}\right\} \tag{26}$$

where γ' denotes the angle of the sidewall ($\gamma' = \gamma - \alpha$), and δ is the wall-soil friction angle called external friction angle. In addition, μ_p is the angle of the slip surface and depends on the wall angle, terrain geometry, and friction angle of the soil; μ_p is determined as a value minimizing the passive soil resistance, P_p. The total passive force, F_{sp}, is obtained by integrating P_p on the sidewall along the $x^{(w)}$ direction as follows:

$$F_{sp} = \int_{-\theta_f}^{\theta_f} P_p(r - h(\theta)\cos\theta)d\theta. \tag{27}$$

On the other hand, active soil resistance P_a is the force acting on the other sidewall pushed by the soil, and is similarly given by:

$$\left.\begin{array}{l}
P_a = \rho g h^2 N_\rho + chN_c + c_a hN_{ca}, \\
N_\rho = \dfrac{C}{2C_a \sin(\mu_a-\alpha)\cos\gamma'}, \\
N_c = \dfrac{\{\sin\mu_a+\cos\mu_a\cot(\mu_a-\phi)\}\cos(\gamma'-\alpha)}{C_a}, \\
N_{ca} = \dfrac{\cos\gamma'-\sin\alpha\cot(\mu_a-\phi)}{C_a}, \\
C_a = \cos\gamma'\{\sin(\gamma'+\delta)+\cos(\gamma'+\delta)\cot(\mu_a-\phi)\},
\end{array}\right\} \tag{28}$$

where, the angle of slip surface μ_a is determined to maximize active soil resistance P_a. The total active force, F_{sa}, is gained similar to (27).

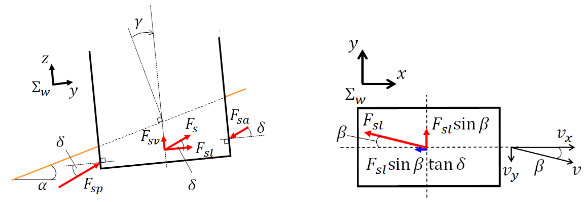

(a) $x - y$ and z components of F_s (b) x and y component of F_s

Fig. 8. x, y, and z components of F_s

Consequently, the total force acting on both sidewalls of the wheel, F_s, is given as follows:

$$F_s = \begin{cases} F_{sa} - F_{sp} & (\beta > 0) \\ F_{sp} - F_{sa} & (\beta < 0) \\ 0 & (\beta = 0). \end{cases} \tag{29}$$

As shown in Fig. 8, the forces acting on the sidewalls along the x, y, and z directions are given by the following equations:

$$F_{xs} = -F_s \cos\delta \sin|\beta| \tan\delta, \tag{30}$$
$$F_{ys} = -F_s \cos\delta \sin\beta, \tag{31}$$
$$F_{zs} = F_s \sin\delta. \tag{32}$$

IV. Slope-Traversing Experiments and Numerical Simulations

To analyze the effects of the rover reconfiguration on the traversability and to evaluate the validation of above-mentioned rover model, slope-traversing experiments and numerical simulations were conducted. In this section, the experimental conditions are first described and the procedure used for the numerical simulations is then given. Subsequently, the results of the numerical simulations are compared to the experimental results, and the validation of the rover model is discussed.

A. Slope-Traversing Experiments

Experimental Setup: Fig. 10 shows the CAD model of the rover test bed on a slope. In this experiment, a four-wheeled rover test bed was used. Each wheel is driven independently and includes a rotary encoder. Furthermore, the attitude of the rover can be changed by manually sliding the wheel-attached section. The specifications of this rover are listed in Table I.

Fig. 10 shows the test field. We used a sandbox 2 [m] in length and 1 [m] in width. It can be jacked up manually for an inclination of up to approximately 20 [deg]. The box was uniformly and loosely covered with Toyoura Standard Sand (dry sand). Toyoura sand is cohesionless and less compressible than natural sand which makes experiments highly repeatable.

The motion of the rover was tracked using a motion capture camera with an accuracy of approximately 10 [mm].

Experimental Conditions: In the experiments, the rover was made to travel a distance of approximately 1 [m] along the $x^{(s)}$ axis. The motor of each wheel was controlled with a constant angular velocity of $r\omega \simeq 20$ [mm/s]. In the first set of experiments, we set the mass of the test bed to 23.8

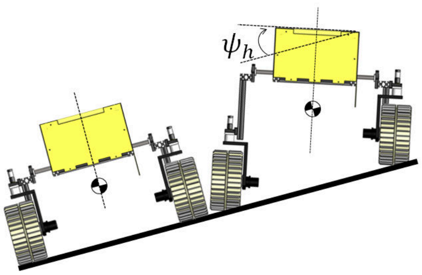

Fig. 9. Rover test bed and its reconfiguration (left: nominal configuration, right: inclined configuration)

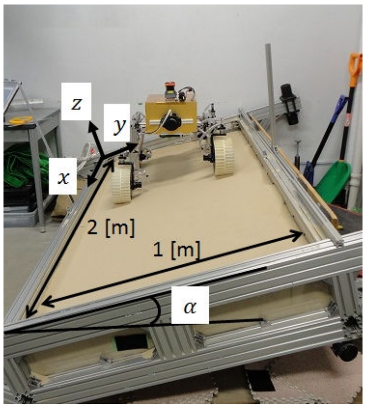

Fig. 10. Test field filled with dry loose sand

[kg]. The roll angle of the test bed, ψ_h, was varied from 0 to 20 [deg] at 5 [deg] intervals. The inclination angle of the sand box was set at 10, 15, and 20 [deg]. In the next set of experiments, we set the test bed mass to 33.8 [kg] and the angle of the slope to 20 [deg]. The roll angle of the test bed was varied from 0 to 20 [deg] with 5 [deg] intervals.

During the experiments, the trajectory of the test bed was obtained and slip ratio s and slip angle β were calculated. These experiments were repeated three times under each condition.

B. Slope-Traversing Simulations

Simulation Procedure: In this simulation, two traversability indexes, the slip ratio and slip angle, were estimated such that forces acting on the rover meet the requirements specified in (8). The simulation procedure is summarized as follows:

1) Input the sand parameters, rover parameters, and initial estimate values of the central wheel sinkages h_{ci}, slip ratio s and slip angle β (i is the wheel number).

TABLE I

SPECIFICATIONS OF THE ROVER TEST BED (NOMINAL CONFIGURATION)

Size [mm]	L800 × W650 × H400
Mass [kg]	23.8 or 33.8
Wheel size [mm]	ϕ200 × W100
Tread [mm]	550
Wheel base [mm]	600
Center of gravity [mm]	L_d = L_u = 275, L_h = 187

2) Calculate the wheel sinkage h'_0 and wheel entry and exit angles θ_f, θ_r.
3) Calculate the normal and shear stresses, σ, τ_t and τ_l, beneath the wheel, and the passive and active resistances, P_p and P_a, on the sidewall.
4) Determine the vertical force of the wheel, F_{zi}.
5) If $F_{zi} - W_i \cos\alpha' > 0$, modify h_{ci} and return to 2).
6) Determine the drawbar pull, F_{xi}, and side force, F_{yi}.
7) If $\Sigma F_{xi} > 0$ or $\Sigma F_{yi} - W \sin\alpha' > 0$, modify s or β and return to 2).
8) Output the slip ratio s and slip angle β.

Simulation Conditions: The simulation conditions are listed in Table II. The numerical simulations were conducted under similar conditions used for the experiments. Table III shows the parameters of the rover and soil used in the simulation. The values of the soil parameters (c, ϕ, ρ, k_c, k_ϕ, n, a_0, and a_1) were determined by Ishigami [21]. The values of the parameters which depend on both the soil and wheel properties (k, λ, c_a and δ) were determined experimentally.

C. Results and Discussion

Fig. 11 shows examples of traversing paths obtained in the experiments drawn in the slope coordinate system Σ_s. It can be seen clearly that the downhill sideslip decreases with increasing roll angle of the test bed.

Fig. 12 shows the experimentally measured and numerically estimated slip ratio s and slip angle β under each condition. As shown in the figures, the absolute value of both the measured slip ratio and slip angle decrease with an increase in the roll angle of the rover over all slopes and weight of the rover. However, these values do not become zero and residual slippages remain, especially over large slope angles.

TABLE II

CONDITIONS OF THE NUMERICAL SIMULATION

	Rover mass [kg]	Roll angle [deg]	Slope angle [deg]
#1	23.8	0 - 20	10
#2	23.8	0 - 20	15
#3	23.8	0 - 20	20
#4	33.8	0 - 20	20

TABLE III

PARAMETERS OF THE NUMERICAL SIMULATION

Parameters	Value	Unit
r	0.097	[m]
b	0.10	[m]
c	0.0	[Pa]
ϕ	38.0	[deg]
ρ	1.49 $\times 10^3$	[kg/m^3]
k_c	0.0	[-]
k_ϕ	122.73	[-]
n	1.703	[-]
a_0	0.40	[-]
a_1	0.15	[-]
k	0.0283	[m]
λ	$2.10s^2 - 1.95s + 0.82$	[-]
c_a	0.0	[Pa]
δ	0.0	[deg]

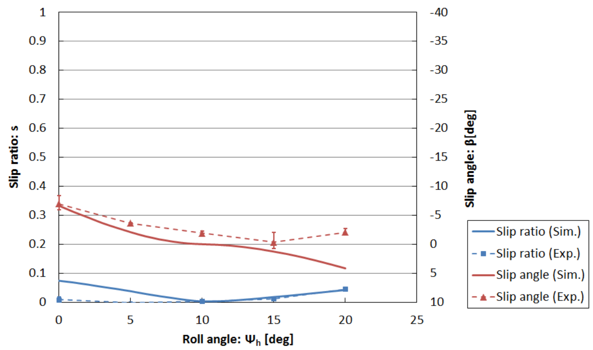

(a) #1: Slope angle, 10 [deg]; rover mass, 23.8 [kg]

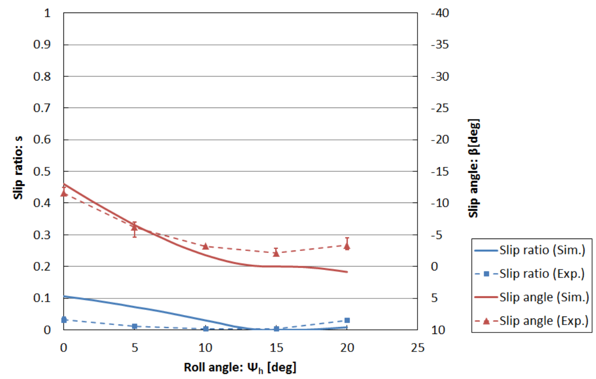

(b) #2: Slope angle, 15 [deg]; rover mass, 23.8 [kg]

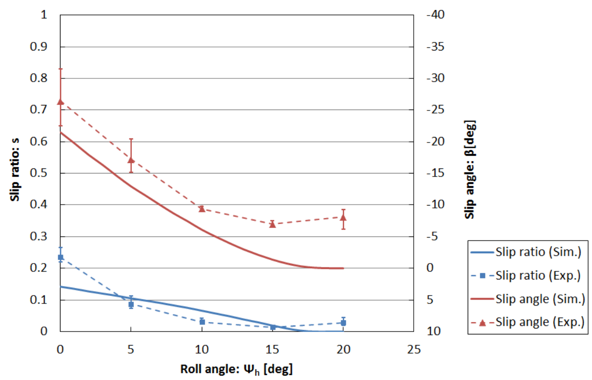

(c) #3: Slope angle, 20 [deg]; rover mass, 23.8 [kg]

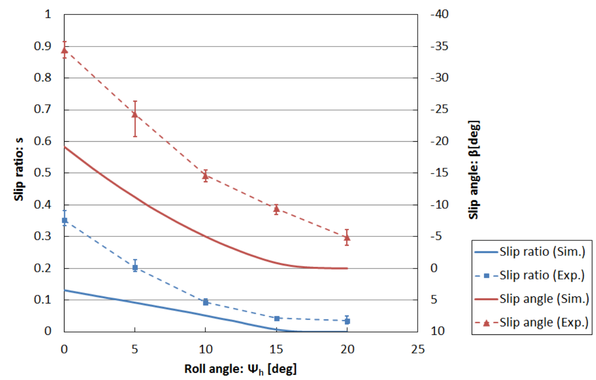

(d) #4: Slope angle, 20 [deg]; rover mass, 33.8 [kg]

Fig. 12. Experimental and simulation results

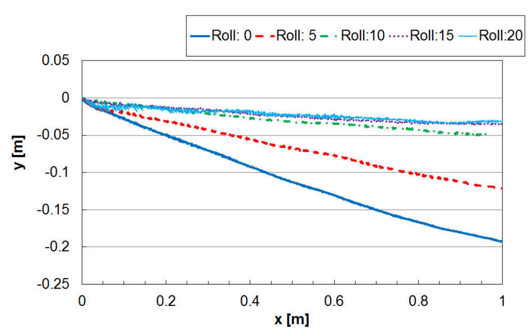

Fig. 11. Experimental traversal paths in slope coordinate (slope angle, 15 [deg]; rover mass, 23.8 [kg])

In the cases of small weight, #1, #2, and #3, the simulated values of the slip ratio and slip angle behave similar to those of the experimental values while $\psi_h < \alpha$. When ψ_h equals α, the rover is in the inclined configuration with the wheels making horizontal contact with the slopes. The simulation estimations for s and β become zero in this case. Furthermore, when ψ_h becomes greater than α, the estimated value of β becomes positive, i.e., the test bed skids toward the uphill direction of the slope. These simulation results differ from the above mentioned experimental results. We assume that these differences between the experimental and simulation results occurred because the proposed model does not consider a "slope failure" phenomenon. When the wheel makes horizontal contact with the slope, the gravitational force acts on the wheel perpendicular to the direction of the lateral shear, as shown in Fig. 13(a). In addition, with the proposed wheel-soil contact model, the forces acting on the sidewalls are considerably lower than forces acting on the bottom, therefore the simulation erroneously estimates the sideslip as zero. In a similar fashion, when $\psi_h > \alpha$, the uphill directional component of the gravitational force increases as depicted in Fig. 13(b), and thus β increases in the uphill direction and s also increase to meet the conditions of (8). On the other hand, the soil beneath the wheel actually moves downhill owing to the rolling of the wheel and the lack of bearing capacity of the soil. Such downhill soil flow generates a downhill sideslip of the rover, and this slope failure is attributed to the above-mentioned residual slippages measured in the experiments.

In the case of large weight #4, although the estimated characteristics of the slip ratio and slip angle trend similar to those of the experimental characteristics, large estimation errors can be seen. One of the reasons for this is a slope failure phenomenon as mentioned above. Another possible factor is errors in the parameters used for the simulations. As shown in Fig 12(d), simulation results underestimated slip ratio s, which therefore means that v_x is overestimated (see (1)). Based on (2), overestimation of v_x provides underestimation of slip angle β. In addition, errors in the slippage

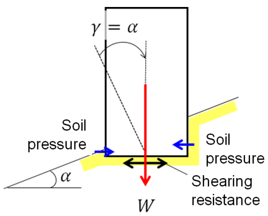

(a) Horizontal wheel

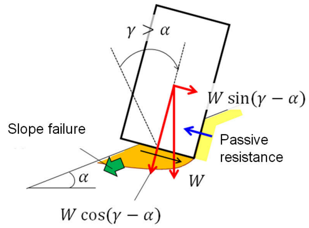

(b) Leaned wheel

Fig. 13. Gravitational forces based on the wheel contact conditions, and a slope failure resulting due to wheel rotation

estimation may result from an orientation error of the test bed. In this study, we assumed that the orientation error is negligible (i.e., the test bed traverses along the $x^{(s)}$ axis); however, the heading of the rover drifted slightly downhill in the experiments under this weight condition.

Based on the discussion above, a slope failure model needs to be introduced into the wheel-soil contact model. Furthermore, the proposed model needs to be extended to allow the change in the yaw angle of the rover and to include slope-ascending and descending cases.

V. Conclusion

In this study, reconfiguration effects of planetary rovers on the traversability over sandy deformable slopes were analyzed based on experiments and numerical simulations. According to the slope traversing experiments, while both longitudinal and lateral slippages can be greatly reduced by tilting the rover in an uphill direction, residual slippages remain, especially over steep slopes. In addition, the results of the numerical simulations showed quantitatively similar trends with the experimental results. The simulation results also indicate that "slope failure" should be incorporated into the proposed rover model for a more accurate modeling of the slope traversing behaviors.

As future research, the slope failure phenomenon has to be studied experimentally under various soil environments and rover specifications in order to combine an appropriate slope failure model into the wheel-soil contact model. Additionally, expanding the rover model from a lateral slope-traversing case to slope-ascent and descent cases is another prospective area of research.

References

[1] S. V. Sreenivasan, and B. H. Wilcox, "Stability and Traction Control of an Actively Actuated Micro-Rover," *Journal of Robotic Systems*, vol.11, no.6, pp.287-502, 1994.

[2] K. Iagnemma, A. Rzepniewski, S. Dubowsky, and P. Schenker, "Control of Robotic Vehicles with Actively Articulated Suspensions in Rough Terrain," *Autonomous Robotics*, vol.14, pp.5-16, 2003.

[3] C. Grand, F. BenAmar, F. Plumet, P. Bidaud, "Stability and traction optimization of reconfigurable vehicles. Application to an hybrid wheel-legged robot," *The Int. Journal of Robotics Research*, vol.23, no.10-11, pp.1041-1058, 2004.

[4] D. Wettergreen, S. Moreland, K. Skonieczny, D. Jonak, D. Kohanbash, and J. Teza, "Design and Field Experimentation of a Prototype Lunar Prospector," *The Int. Journal of Robotics Research*, vol.29, no. 2, pp.1550-1564, 2010.

[5] M. G. Bekker, *Introduction to Terrain-Vehicle Systems*, Ann Arbor, MI, USA, University of Michigan Press, 1969.

[6] J. Y. Wong, *Theory of Ground Vehicles*, John Wiley & Sons Inc., 1978.

[7] K. Iagnemma, H. Shibly, and S. Dubowsky, "On-Line Terrain Parameter Estimation for Planetary Rovers," *Proc. of the 2002 IEEE Int. Conf. on Robotics and Automation*, pp.3142-3147, 2002.

[8] Y. Favaedi, A. Pechev, M. Scharringhausen, and L. Richter, "Prediction of Tractive Response for Flexible Wheels with Application to Planetary Rovers," *Journal of Terramechanics*, vol.48, issue 3, pp.199-213, 2011.

[9] B. Trease, R. Arvidson, R. Lindemann, K. Bennett, F. Zhou, K. Iagnemma, C. Senatore, and L. V. Dyke, "Dynamic Modeling and Soil Mechanics for Path Planning of the Mars Exploration Rovers," *Proc. of the ASME 2011 Int. Design Engineering Tech. Cong. & Computers and Information in Engineering Conf.*, 2011.

[10] K. Yoshida and H. Hamano, "Motion Dynamics of a Rover with Slip-Based Traction Model," *Proc. of the 2002 IEEE Int. Conf. on Robotics and Automation*, pp.3155-3160, 2002.

[11] G. Ishigami, A. Miwa, K. Nagatani, and K. Yoshida, "Terramechanics-based Model for Steering Maneuver of Planetary Exploration Rovers on Loose Soil," *Journal of Field Robotics*, vol.24, no.3, pp.233-250, 2007.

[12] K. Nagatani, A. Ikeda, K. Sato, and K. Yoshida, "Accurate Estimation of Drawbar Pull of Wheeled Mobile Robots Traversing Sandy Terrain Using Build-in Force Sensor Array Wheel," *Proc. of the 2009 IEEE/RSJ Int. Conf. on Intelligent Robots and Systems*, pp.2373-2378, 2009.

[13] A. R. Reece, "Principles of Soil-Vehicle Mechanics," *Proc. of the Instn of Mech. Engrs*, vol.180, part 2A, no.2, pp.45-66, 1965-1966.

[14] C. Senatore and C. Sandu, "Off-road Tire Modeling and the Multi-pass Effect for Vehicle Dynamics Simulation," *Journal of Terramechanics*, vol.48, issue 4, pp.265-276, 2011.

[15] J. Y. Wong and A. R. Reece, "Prediction of Rigid Wheel Performance based on the Analysis of Soil-Wheel Stress, Part *I*," *Journal of Terramechanics*, vol.4, no.1, pp.81-98, 1967.

[16] Z. Janosi and B. Hanamoto, "The Analytical Determination of Drawbar Pull as a Function of Slip for Tracked Vehicles in Deformable Soils," *Proc. of the First Int. Conf. on the Mechanics of Soil Vehicle Systems*, Turin, 1961.

[17] T. H. Tran, N. M. Kwok, S. Scheding, and Q. P. Ha, "Dynamic Modelling of Wheel-Terrain Interaction of a UGV," *Proc. of the 3rd Annual IEEE Conf. on Automation Science and Engineering*, pp.369-374, 2007.

[18] J. Y. Wong and C. F. Chiang, "A General Theory for Skid Steering of Tracked Vehicles on Firm Ground," *Proc. of the Instn of Mech. Engrs*, vol.215, part D, pp.343-355, 2001.

[19] E. McKyes, "*Soil Cutting and Tilage*," Elsevier, 1985.

[20] A. R. Reece, "The Fundamental Equation of Earthmoving Mechanics," *Proc. of the Instn of Mech. Engrs*, vol.179, part 3F, pp.16-22, 1964.

[21] G. Ishigami, "Terramechanics-based Analysis and Control for Lunar/Planetary Exploration Robots," Ph. D Thesis, Tohoku University, Japan, 2008.